1 **The characteristics of the 2022 Tonga volcanic tsunami in the Pacific Ocean**

2 Gui Hu[1], Linlin Li[1,2], Zhiyuan Ren[3], Kan Zhang[1]

3 1. Guangdong Provincial Key Laboratory of Geodynamics and Geohazards, School of Earth Sciences
4 and Engineering, Sun Yat-sen University, Guangzhou, China

5 2. Southern Marine Science and Engineering Guangdong Laboratory (Zhuhai), Zhuhai, China

6 3. Department of Civil and Environmental Engineering, National University of Singapore, Singapore.

7 *Correspondence to:* Linlin Li (lilinlin3@mail.sysu.edu.cn)

8 **Abstract.** On 15th January 2022, an exceptional eruption of Hunga Tonga–Hunga Ha'apai volcano
9 generated atmospheric and tsunami waves that were widely observed at oceans globally, gaining a
10 remarkable attention to scientists in related fields. The tsunamigenic mechanism of this rare event
11 remains an enigmatic due to its complexity and lacking of direct underwater observations. Here, to
12 explore the tsunamigenic mechanisms of this volcanic tsunami event and its hydrodynamic processes in
13 the Pacific Ocean, we conduct tsunami waveform and spectral analyses of the waveform recordings at
14 116 coastal gauges and 38 deep-ocean buoys across the Pacific Ocean. Combined with the constraints of
15 some representative barometers, we obtain the plausible tsunamigenic origins during the volcano activity.
16 We identify four distinct tsunami wave components generated by air-sea coupling and seafloor crustal
17 deformation. Those tsunami components are differentiated by their different propagating speeds or period
18 bands. The first-arriving tsunami component with ~80–100 min period was from shock waves spreading
19 at a velocity of ~1000 m/s in the vicinity of the eruption. The second component with extraordinary
20 tsunami amplitude in deep sea was from Lamb waves. The Lamb wave with ~30–40 min period radically
21 propagated outward from the eruption site with spatially decreasing propagation velocities from ~340
22 m/s to ~315m/s. The third component with ~10–30 min period was probably from some atmospheric
23 gravity wave modes propagating faster than 200 m/s but slower than Lamb waves. The last component
24 with ~3–5 min period originated from partial caldera collapse with dimension of ~0.8–1.8 km.
25 Surprisingly, the 2022 Tonga volcanic tsunami produced long oscillation in the Pacific Ocean which is
26 comparable with those of the 2011 Tohoku tsunami. We point out that the long oscillation is not only
27 associated with the resonance effect with the atmospheric acoustic-gravity waves, but more importantly
28 the interactions with local bathymetry. This rare event also calls for more attention to the tsunami hazards
29 produced by atypical tsunamigenic source, e.g., volcanic eruption.

1. Introduction

On 15 January 2022 at 04:14:45 (UTC), a submarine volcano erupted violently at the uninhabited Hunga Tonga-Hunga Ha'apai (HTHH) island at 20.546°S 175.390°W (USGS, 2022). The volcano is located ~67 km north of Nuku'alofa, the capital of Tonga (NASA, 2022) (Figure 1). The blasts launched plumes of ash, steam, and gas ~58 km high into stratosphere (Yuen et al., 2022) which not only blanketed nearby islands in ash (Duncombe, 2022; NASA, 2022), but caused various atmospheric acoustic-gravity wave modes (AGWs) of various scales, e.g., Lamb waves from atmospheric surface pressure disturbance associated with the eruption (Liu and Higuera, 2022; Adam, 2022; Kubota et al., 2022; Matoza et al., 2022). Tsunami with conspicuous sea level changes were detected by coastal tide gauges and Deep-ocean Assessment and Reporting of Tsunamis (DART) buoy stations in the Pacific (Figure 1), the Atlantic, and Indian Oceans as well as the Caribbean and Mediterranean seas (Carvajal et al., 2022; Kubota et al., 2022; Ramírez-Herrera et al., 2022), while the large waves were mainly concentrated in the Pacific Ocean, like coastlines of New Zealand, Japan, California, and Chile (Carvajal et al., 2022). The event caused at least 3 fatalities in Tonga. Two people drowned in northern Peru when ~2 m destructive tsunami waves inundated an island in the Lambayeque region, Chile (Edmonds, 2022).

Satellite images revealed that the elevation of HTHH island has gone through dramatic change before and after the mid-January 2022 eruption. Previously, after the 2015 eruption, the two existing Hunga Tonga and Hunga Ha'apai Islands were linked together. The volcanic island rose 1.8 km from the seafloor where it stretched ~20 km across and topped a underwater caldera ~5 km in diameter (Garvin et al., 2018; NASA, 2022). After the violent explosion on 15 January 2022, the newly formed island during 2015 was completely gone, with only small tips left in far southwestern and northeastern HTHH island (NASA, 2022). HTHH volcano lies along the northern part of Tonga–Kermadec arc, where the Pacific Plate subducts under the Indo-Australian Plate (Billen et al., 2003). The convergence rate (15~24 cm/year) between the Tonga-Kermadec subduction system and the Pacific plate is among the fastest recorded plate velocity on Earth, forming the second deepest trench around the globe (Satake, 2010; Bevis et al., 1995). The fast convergence rate contributes to the frequent earthquakes, tsunamis and volcanic eruptions in this region historically (Bevis et al., 1995). The 2022 HTHH volcano is part of a submarine-volcano chain that extends all the way from New Zealand to Fiji (Plank et al., 2020). HTHH volcano had many notable eruptions before 2022 since its first historically recorded eruption in 1912, i.e., in 1937, 1988,

59   2009, 2014-2015 (Global Volcanism Program, https://volcano.si.edu).
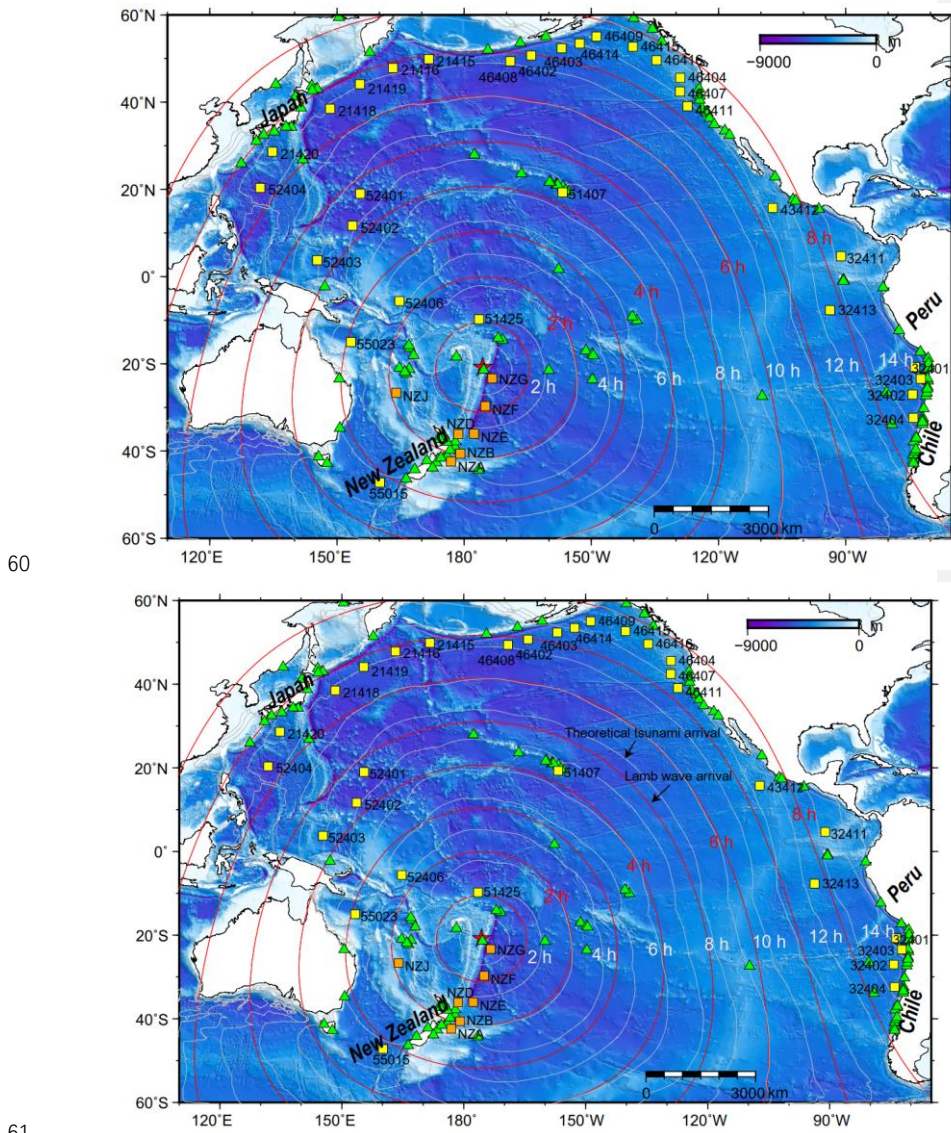
Figure 1. The spatial distribution of the eruption site (red star), DART stations (squares), tide gauges (triangles) and the calculated tsunami arrival times. White contours indicate the modelled arrival times of conventional tsunami. Red contours indicate the estimated arrival times of Lamb waves (see how we derive these contours in section 3.1).

The 2022 HTHH eruption is the first volcanic event which generates worldwide tsunami signatures since the 1883 Krakatau event (Matoza et al., 2022; Self and Rampino, 1981; Nomanbhoy and Satake, 1995).

68 The tsunamigenic mechanism of this rare volcanic eruption-induced tsunami is still poorly understood

69 due to its complex nature and the deficiencies of near-field seafloor surveys. Various tsunami generation

70 mechanisms have been proposed so far based on the observations of ground-based and spaceborne

71 geophysical instrumentations (Kubota et al., 2022; Matoza et al., 2022; Carvajal et al., 2022). The

72 mechanisms are closely associated with the air-sea coupling with atmospheric waves. Atmospheric

73 waves propagating in the atmospheric fluid with different speeds are generated by different physical

74 mechanisms (E. E. Gossard and W. H. Hooke, 1975). Nonlinearities in the process may lead to the

75 formation of shock-wave and period lengthening. The balance between gravity and buoyancy causes

76 gravity waves. The acoustic wave propagate by atmospheric fluid compression and rarefaction (Matoza

77 et al., 2022). The most-mentioned mechanism of the tsunami is the fast-traveling atmospheric Lamb wave

78 generated by the atmospheric pressure rise of ~2 hPa during the eruption. The Lamp wave circled the

79 Earth for several times with travelling speed close to that of the sound wave in the lower atmosphere,

80 leading to globally observed sea level fluctuations (Adam, 2022; Duncombe, 2022; Kubota et al., 2022;

81 Matoza et al., 2022) (Figure 1). The second mechanism is suggested to be a variety of other acoustic-

82 gravity wave modes (Adam, 2022; Matoza et al., 2022; Themens et al., 2022; Zhang et al., 2022). The

83 third mechanism may be related to the seafloor crustal deformation induced by one or more volcanic

84 activities in the vicinity of the eruption site (e.g., pyroclastic flows, partial collapse of the caldera)

85 (Carvajal et al., 2022) , which are more responsible for the near-field tsunamis with theoretical tsunami

86 speeds.

87 To investigate the possible tsunamigenic mechanisms and detailed hydrodynamic behaviors of this rare

88 volcanic tsunami event, in this study, we collect, process and analyze the sea level measurements from

89 116 tide gauge and 38 DART buoys in the Pacific Ocean (shown in Figures 1 and 2). We first do statistical

90 analysis of the tsunami waveforms to estimate the propagating speed of the Lamb wave and to understand

91 the tsunami wave characteristics in the Pacific Ocean through demonstrating the tsunami wave properties,

92 i.e., arrival times, wave heights and durations. We then conduct wavelet analysis for representative DART

93 buoys and tide gauges respectively to explore tsunamigenic mechanisms of the event and to better

94 understand its hydrodynamic processes in the Pacific Ocean. Aided by wavelet analysis of corresponding

95 barometers near the selected DART buoys and comparison with tsunami records of the 2011 Tohoku

96 tsunami, we are able to piece together all the analysis and demonstrate that the 2022 HTHH tsunami was

带格式的: 字体: 10 磅

带格式的: 字体: 10 磅, 字体颜色: 文字 1

带格式的: 字体颜色: 文字 1, 非突出显示

带格式的: 字体: 10 磅

带格式的: 字体: 10 磅, 字体颜色: 文字 1

带格式的: 字体颜色: 文字 1, 非突出显示

带格式的: 字体颜色: 文字 1

97   generated by air-sea coupling with a wide range of atmospheric waves with different propagating

98   velocities and period bands, and seafloor crustal deformation associated with the volcanic eruption. We

99   demonstrate as well that the tsunami was amplified at the far-field Pacific coastlines where the local

100   bathymetric effects play a dominant role in tsunami scale.

101   **2.   Data and Methods**

102   **2.1 Data**

103   We collected high-quality sea level records across the Pacific Ocean at 38 DART buoys (in which 31

104   stations from https://nctr.pmel.noaa.gov/Dart/, 7 stations from https://tilde.geonet.org.nz/dashboard/) and

105   116 tide gages from IOC (The Intergovernmental Oceanographic Commission, http://www.ioc-

106   sealevelmonitoring.org) (Figure 1). The epicentral distances of tide gauges and DART buoys range

107   between 74–10790 km and 375–10414 km, respectively. The sampling rates of DART buoys are

108   changing over time. Passing of tsunami event generally can trigger the DART system to enter its high

109   frequency sampling mode (15 seconds or 1 min) from normal frequency mode (15 min)

110   (www.ndbc.noaa.gov/dart). In contrast, sampling rates of normal tide gauges at coasts are uniform with

111   sampling interval of 1 min. The sampling interval of both DART and tide gauges is preprocessed to 15

112   seconds. Firstly, we eliminate abnormal spikes and fill gaps by linear interpolation. Secondly, we applied

113   a fourth-order Butterworth-Highpass filter with a cut-off frequency of 3.5 e-5 Hz (~ 8 hours) to remove

114   the tidal components (Figure 2) (Heidarzadeh and Satake, 2013). After the two steps, quality control step

115   is conducted to select high-quality data, in which we delete waveforms with spoiled data or massive data

116   loss due to equipment failure, or with the maximum tsunami heights of tide gauges less than 0.2 m, then

117   the selected data will be ready for further statistics and spectral analysis. We also collect and analyze the

118   atmospheric pressure disturbance data recorded by some representative barometers. The sampling rates

119   of the barometers is generally uniform with a sampling rate of 1 min except for some stations in New

120   Zealand with interval of 10 min. Considering the sample rate, we employ a fourth-order Butterworth-

121   Bandpass filter with period ranging between 2–150 min for wavelet analysis of the barometers with 1

122   min sample rate, while we apply the fourth-order Butterworth-Bandpass filter with range of 30–150 min

123   to long-period waveform display based on two reasons. (1) The barometer data we use for the analysis

124   include some in New Zealand with 10 min sample rate; (2) Filtering out the short-period waves helps

5

125 highlight long-period tsunami wave components.

126 The tsunami waveforms recorded by DART buoys which are installed offshore in the deep water are

127 expected to contain certain characteristics of the tsunami source (Wang et al., 2020, 2021). The

128 waveforms recorded by tide gauge distributed along coastlines are significantly influenced by local

129 bathymetry/topography which are used for investigating bathymetric effect on tsunami behaviors

130 (Rabinovich et al., 2017, 2006; Rabinovich, 2009). Therefore, we use the DART data for source-related

131 analysis and choose some tide gauge data to investigate the tsunami behaviors at the Pacific coastlines.

132
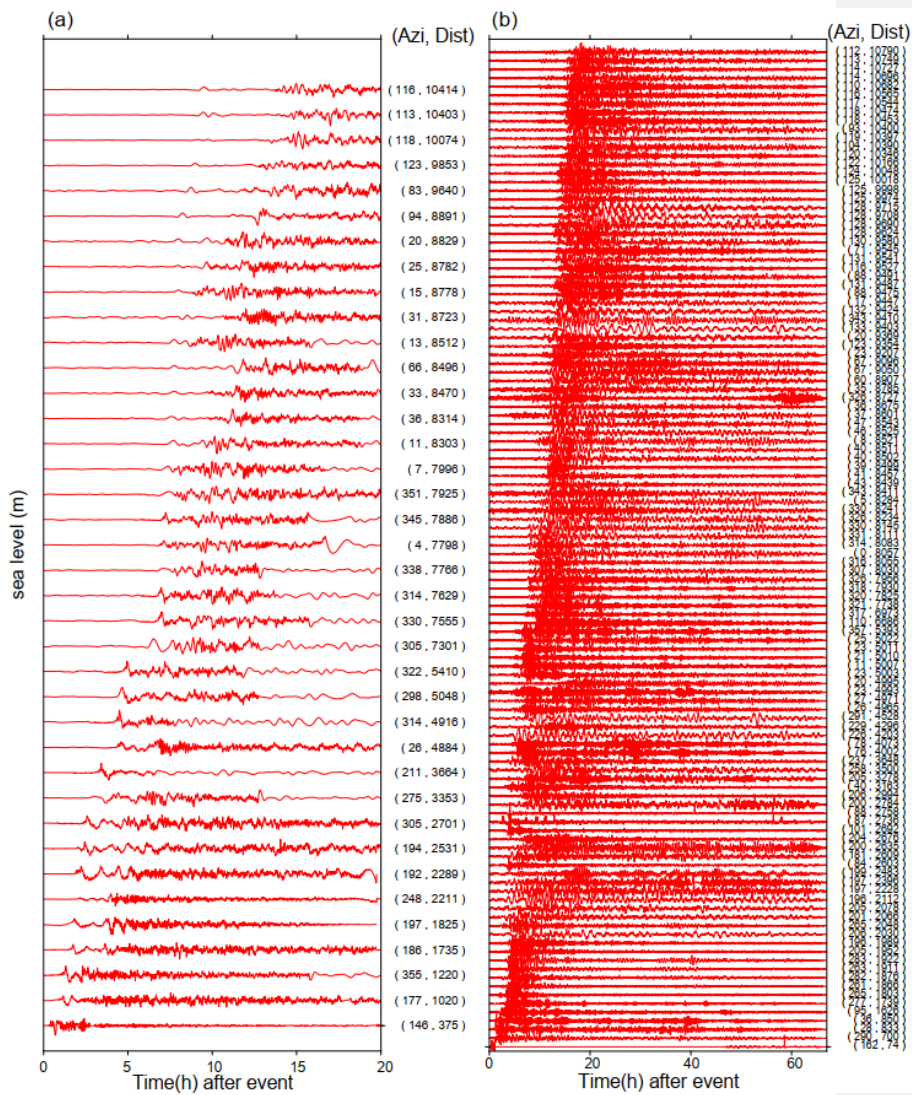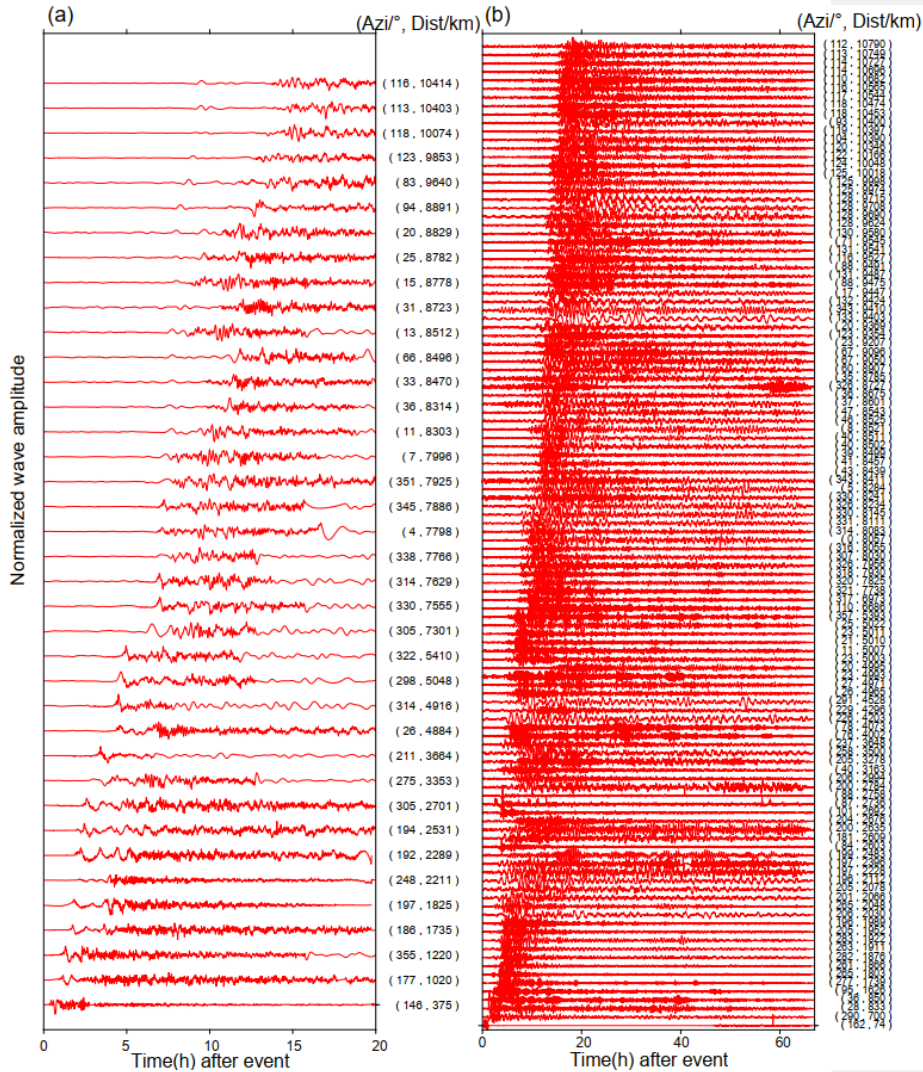
Figure 2. Detided tsunami waveforms at (a) DART buoys and (b) tide gauges. Waveforms in both subplots are shown in ascending distance. Azi stands for azimuth.

2.2 Tsunami Modelling

We use a numerical tsunami modelling package JAGURS (Baba et al. 2015) to simulate the tsunami propagation of the 2022 HTHH event and obtain the theoretical tsunami arrival time based on the shallow water wave speed (white contours in Figure 1). The code solves linear Boussinesq-type equations in a spherical coordinate system using a finite difference approximation with the leapfrog method. We specify

7

带格式的: 字体: (中文) +中文正文 (等线), 10 磅, 加粗, 字体颜色: 黑色, 图案: 清除 (自定义颜色(RGB(247,247,247)))

141 a unit Gaussian-shaped vertical sea surface displacement at the volcanic base as the source of

142 conventional tsunami. For a unite source i with center at longitude φ_i and latitude θ_i, the

143 displacement distribution $Zi(\varphi, \theta)$ can be expressed as:

144 $$Zi(\varphi, \theta) = exp[-\frac{(\varphi-\varphi_i)^2+(\theta-\theta_i)^2}{2\sigma}] \tag{1}$$

145 Where we set characteristic length σ as 5 km (NASA, 2022). The bathymetric data is resampled from the

146 GEBCO 2019 with 15 arc-sec resolution (The General Bathymetric Chart of the Oceans, downloaded

147 from https://www.gebco.net).

2.3 Spectral Analysis of Tsunami Waves

149 To investigate the temporal changes of the dominant wave periods, we conduct continuous wavelet

150 transformation (frequency-time) analyses for some representative DART buoys, tide gauges and

151 barometers, in which wavelet Morlet mother function is implemented (Kristeková et al., 2006). The first

152 32-hour time series of DART buoys and barometers after the eruption (at 04:14:45 on 15 January 2022)

153 are used for source-related wavelet analysis. The first 48-hour time series of tide gauges after the eruption

154 are employed for hydrodynamics-related wavelet analysis at coastlines. We adopt the Averaged-Root-

155 Mean-Square (ARMS) method as a measure of absolute average tsunami amplitude with a moving time

156 window of 20 min to calculate the tsunami duration (Heidarzadeh and Satake, 2014). We define the time

157 durations as the time period where ARMS levels of tsunami waves are above those prior to the tsunami

158 arrivals.

3. Results

3.1 The decreasing propagation velocities of the Lamb Wave

161 Although many types of atmospheric waves were generated by the 2022 HTHH eruption, the most

162 prominent signature was the Lamb waves which were globally observed by ground-based and spaceborne

163 geophysical instrumentations (Kulichkov et al., 2022; Liu et al., 2022; Lin et al., 2022; Matoza et al.,

164 2022; Themens et al., 2022; Adam, 2022; Kubota et al., 2022). Interestingly, we notice that a wide range

165 of the velocities from 280 m/s to 340 m/s were proposed through observations and Lamb wave modelling

166 (e.g., Kubota et al., 2022; Lin et al., 2022; Matoza et al., 2022; Themens et al., 2022). The travelling

167 velocity of Lamb waves in real atmosphere is affected by temperature distributions, winds and dissipation

168 (Otsuka, 2022). To investigate whether the propagation speeds of the lamb wave change in space and

169 time, we analyze the waveforms recorded by the DART buoys in the Pacific Ocean. DART buoy with

170 pressure sensor deployed at the ocean's bottom records the sea level change that is transferred from

171 pressure records in Pascals, instead of direct water height. For the 2022 HTHH tsunami event, the

172 pressure fluctuation at DART buoy is a superposition of the pressure changes caused by tsunami and the

173 Lamb wave (Kubota et al., 2022). The Pacific DART buoys recorded the most discernible air-sea

174 coupling pulse in deep ocean with Lamb waves that arrived earlier than the theoretical tsunamis (Figure

175 1). The tsunami waveforms recorded by tide gauges did not clearly detect the tsunami signals associated

176 with the lamb Lamb waves, therefore not sufficient for further analysis (Figure 2). Thus, we estimate the

177 speed of Lamb waves using the waveforms recorded by the Pacific DART buoys. The Lamb wave

178 arrivals are limited within arrival time range from possible velocities of 280–340 m/s. The time points at

179 which the tsunami amplitudes first exceed 1 e-4 m above sea level are defined as Lamb wave arrivals.

180 By carefully fitting the arrivals with different constant velocities, we illustrate the velocities of Lamb

181 wave were generally uniform, but slightly decrease with the increase of propagation distance (Figure 3).

182 The Lamb waves initially propagated radially at speed of ~340 m/s before slowing to ~325 m/s after

183 reaching ~3400 km, and further decreasing to ~315 m/s at 7400 km. In an isothermal troposphere

184 assumption, the phase velocity of the Lamb wave (C_L) can be estimated with the following equation

185 (Gossard and Hooke, 1975):

186 $$C_L = \sqrt{\frac{\gamma \cdot R \cdot T}{M}} \qquad\qquad (2)$$

187 Where γ =1.4 (air specific heat ratio corresponding to atmospheric temperature), R = 8314.36 J kmol-1

188 K-1 (the universal gas constant), M = 28.966 kg kmol-1 (molecular mass for dry air) are constant for the

189 air, T is the absolute temperature in kelvin. Thus, Lamb wave velocity is mainly affected by the air

190 temperature, meaning the travelling velocity of lamb waves might decrease when propagating from

191 regions with high temperature towards those with low temperatures, e.g., the north pole. By assuming a

192 set of possible temperatures in January (Table 1), we calculated the velocities C_L could range between

193 312–343 m/s when temperatures vary between -30–20 °C. Therefore, the decreased velocity of the Llamb

194 waves could be a consequence of cooling of the air temperature.
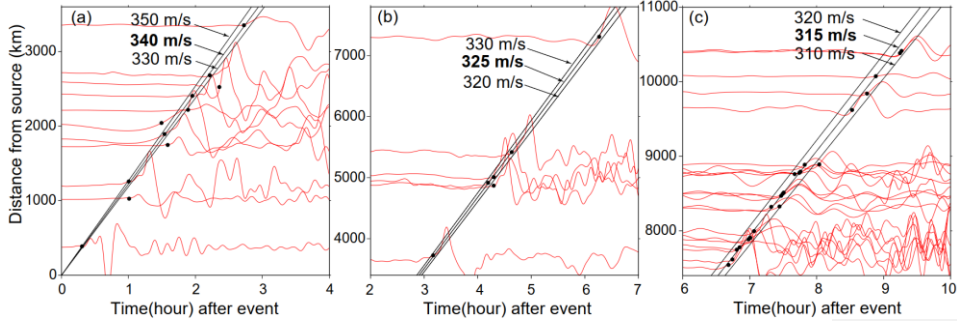
Figure 3. Fitting the arrival times of normalized Lamb waveforms with different velocities. Black dots mark the arrival times of the Lamb waves. Black lines represent velocities.

Table 1. Estimated Lamb wave velocities in an isothermal troposphere assumption

Celsius temperature (°C)	thermodynamic temperature (K)	C_L (m/s)
20	293.15	343.14
10	283.15	337.23
0	273.15	331.21
-10	263.15	325.19
-20	253.15	318.86
-30	243.15	312.49

3.2 Tsunami features observed by DART buoys and Tide gauges

The statistics of tsunami heights and arrival times recorded at 38 DART buoys and 116 tide gauges across the Pacific Ocean are used to interpret the tsunami characteristics. The comparison of the statistical characters between DART and tide gauge observations yields some useful information of the hydrodynamic process of tsunami propagation and help identify tsunami wave components with different traveling velocities.

The average value of the maximum tsunami wave height (trough-to-crest) for the 116 tide gauge stations is ~1.2 m. Figure 4a shows tide gauges with large tsunami heights exceeding 2 m are mainly distributed in coastlines with complex geometries (Figure S1a), such as gauges at New Zealand, Japan, and north and south America. For example, the largest tsunami height among tide gauges is 3.6 m at a bay-shaped coastal area Chañaral in Chile (Figure S1b). In sharp contrast to tide gauges, the maximum tsunami heights of most Pacific DART buoys are less than 0.2 m. The largest tsunami height in the DART buoys is only ~0.4 m recorded at the nearest one, 375 km from the volcano (Figure 4b). The comparison between DART buoys and tide gauges indicate that the direct contribution of air-sea coupling to the tsunami

10

heights is probably in the level of tens of centimeters (Kubota et al., 2022). The meter-scale tsunami heights at the coastlines suggest the bathymetric effect could play a major role during tsunami propagation. In respect to the arrival of maximum tsunami waves, the time lags between Lamb waves and the maximum heights of tide gauges mainly range between ~0–10 h (Figure 4c). The delayed times of ~10 h are observed in New Zealand, Hawaii, and west coast of America (Figure 4c), suggesting the interaction between tsunami waves and local topography/bathymetry delays the arrival of the maximum waves (e.g., Hu et al., 2022). For example, the delayed maximum tsunami height can be attributed to the edge waves (Satake et al., 2020) and resonance effect (Wang et al., 2021) from tsunami interplays with bays/harbors, islands, and continental shelves of various sizes. The significant regional dependence of the coastal tsunami heights and the time lags of the maximum tsunami waves can be attributed to the complexity of local bathymetry, such as continental shelves with different slopes, and harbor/bay with different shapes and sizes (Satake et al., 2020). On the other hand, since the DART records are less influenced by bathymetric variation in space, the first waves in DART buoys are supposed to be the maximum tsunami waves as observed in the 2011 Tohoku tsunami event (Heidarzadeh and Satake, 2013). However, we observe the inconsistency between the arrivals of the Lamb waves and the maximum tsunami heights (Figure 4d). The time lags of the maximum waves of DART buoys present a coarsely increasing tendency with the increasing distance from the volcano, which indicates the contribution of other tsunami generation mechanism propagating with a uniform but lower speed than Lamb wave.

带格式的: 字体: 10 磅, 字体颜色: 文字 1

带格式的: 字体: 10 磅, 字体颜色: 文字 1

带格式的: 字体: 10 磅, 字体颜色: 文字 1

带格式的: 字体: 10 磅, 字体颜色: 文字 1

带格式的: 字体: 10 磅, 字体颜色: 文字 1
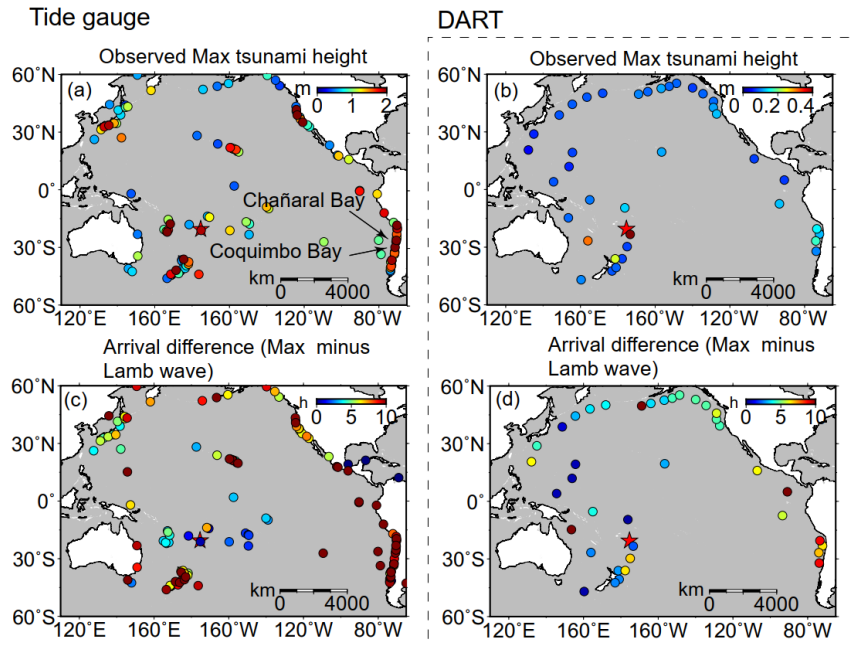
Figure 4. The spatiotemporal signatures of the 2022 HTHH tsunami across the Pacific Ocean. (a) Observed the maximum tsunami height (trough-to-crest height) of tide gauges. (c) Arrival differences between the maximum tsunami height of tide gauges and Lamb waves. (b) and (d) are the same as (a) and (c) but for DART buoys.

3.3 Tsunami components identified from wavelet analysis

The statistical analysis of tsunami waveforms at tide gauges and DART buoys suggest the tsunami waves likely contain several components with different source origins. To further identify these tsunami components, we conduct wavelet analysis for tsunami waveforms recorded by representative DART buoys and air pressure waveforms recorded by selected barometers. We demonstrate the analysis result through the frequency-time (f-t) plot of wavelet which shows how energy and period vary at frequency and time bands (Figure 5 and Figure 6). Tsunami components have clear signatures in all f-t plots as the energy levels are quite large when they arrive. Figure 5 shows the wavelet analysis of six DART buoys located in the vicinity of the eruption site (<3664 km). Figure 6 show the wavelet analysis of ten DART buoys located in the Pacific rim which are far away from the source location. We observe three interesting phenomena: 1) most of the tsunami wave energy is concentrated in four major period bands, i.e., 3–5 min, ~10–30 min, ~30–40 min, and ~80–100 min 80–100 min, 10–30 min, 30–40 min, and 3–5 min; 2)

带格式的: 字体: 10 磅, 字体颜色: 文字 1

12

The significant tsunami component with period band of 3-5 mins are recorded by stations between the eruption site and the north tip of the New Zealand~~The stations with 3-5 mins wave periods are mainly located in the vicinity of the volcano site~~; 3) There exists one exceptional tsunami component with longer wave period of ~80–100 min, mainly recorded in the Tonga, the New Zealand and Hawaii, ~~in the near source region~~ which travels even faster than the ~~lamb~~ Lamb waves.

To further explore the source mechanism of these tsunami components, we take advantage of the published information related to different propagating velocities of atmospheric gravity waves (Kubota et al., 2022) and add four kinds of propagating velocities as criteria to differentiate the tsunami arrivals from different sources (Figure 5 and Figure 6). The first reference speed is 1000 m/s related to the radically propagating atmospheric shock waves near the source region (Matoza et al., 2022; Themens et al., 2022). The second one is the velocities of Lamb wave ranging between 315–340 m/s derived from the aforementioned analysis in section 3.1 (Figure 3). The third one is 200 m/s corresponding to the lower limit of atmospheric gravity wave modes other than Lamb waves which were also excited by the volcanic eruptions (Kubota et al., 2022). The last is the arrival time of conventional tsunami given by tsunami modelling (Figure 1). The theoretical velocity of conventional tsunami is significantly nonuniform spatially as compared with those of the atmospheric waves. The conventional tsunami propagation speed is determined by the water depth along the propagation route. The velocity of non-dispersion shallow-water waves (C_H) in the ocean is given by:

$$C_H = \sqrt{g.H} \tag{3}$$

Where g is gravity acceleration (9.81m/s^2), H is the water depth. The propagation velocities of tsunami are ~296–328 m/s in the deepest trenches on earth (i.e., ~11 km in Mariana Trench and ~9 km in Tonga Trench). The velocities decrease quickly to only ~44 m/s at ~200 m depth along the edge of continental shelf. With the average depth of ~4–5 km, the average velocities in the Pacific Ocean range between ~198–221 m/s. Thus, theoretical tsunami velocities present significant slowness and variability. We delineate the arrival times of the four reference speeds in Figures 5 and 6. ~~For each panel of the figures, from left to right, the solid vertical white lines mark velocity of 1000 m/s. The solid vertical red lines mark the arrival of Lamb waves. The dashed vertical white lines mark lower limit of gravity waves' velocity of 200 m/s. The dashed vertical black lines represent the calculated theoretical tsunami arrivals. Horizontal white dashed lines mark two reference periods of 10 min and 30 min.~~

277 One particularly remarkable phenomenon is that the wave component with period of ~80–100 min

278 propagated at a very fast speed of ~1000 m/s in the vicinity of the HTHH site, i.e., New Zealand and

279 Hawaii (e.g., stations 52406, NZJ, NZE, 51425 in Figure 5, and 51407 in Fig. 6). We infer that the

280 tsunami component within ~80–100 min period band was likely produced by the atmospheric shock

281 waves during the initial stage of the volcanic eruption and spatially only cover the near-source region.

282 To verify this observation, we select 16 representative barometers located in the near-source region and

283 far-field area for wavelet analysis (see the locations in Figure 5 and Figure 6). Figure 7 shows the

284 waveforms of atmospheric pressure at selected locations and Figure 8 provides the frequency-time (f-t)

285 plot of wavelet analysis of some representative barometers. Interestingly, we are able to discern the air

286 pressure pulses prior to Lamb waves at barometers in New Zealand (the two columns on the left in Figure

287 7), although such signals are not detectable in waveforms recorded by barometers far from the source

288 (the two columns on the right in Figure 7). The spatial distribution of such unusual pressure changes

289 suggest that the fast travelling shock waves were only limited in the near-source region, as reflected in

290 the travelling ionospheric disturbances (Matoza et al., 2022; Themens et al., 2022). Additionally, we also

291 see that the long period signals of ~80–100 min appear in DART buoys far away from the eruption site.

292 Such signals may be related with the long-period gravity waves (Matoza et al., 2022).

293 The tsunami components at period band of ~30–40 min can be readily associated with Lamb waves

294 because the arrival times of tsunami waves and Lamb waves have excellent match, as shown in the

295 tsunami data recorded by DART buoys (e.g., NZJ and 51425 in Figure 5; 51407, 32401 and 32413 in

296 Figure 6) and pressure data by barometers (Figure 8).

297 For the tsunami components with the period band of ~10–30 min, although the arrivals of ~10–30 min

298 tsunami components cover some theoretical tsunami arrival times, they do not consistently match. The

299 tsunami components occurring within the time period between Lamb waves and the lower gravity waves'

300 velocities has a good agreement with the velocity range of several atmospheric gravity wave modes

301 (Matoza et al., 2022; Themens et al., 2022; Kubota et al., 2022). Similarly, the air pressure data also show

302 energy peaks at ~10–30 min period band, which is consistent with the tsunami data (Figure 8). Such

303 consistency further verifies the contribution of atmospheric gravity waves to the volcanic tsunami.
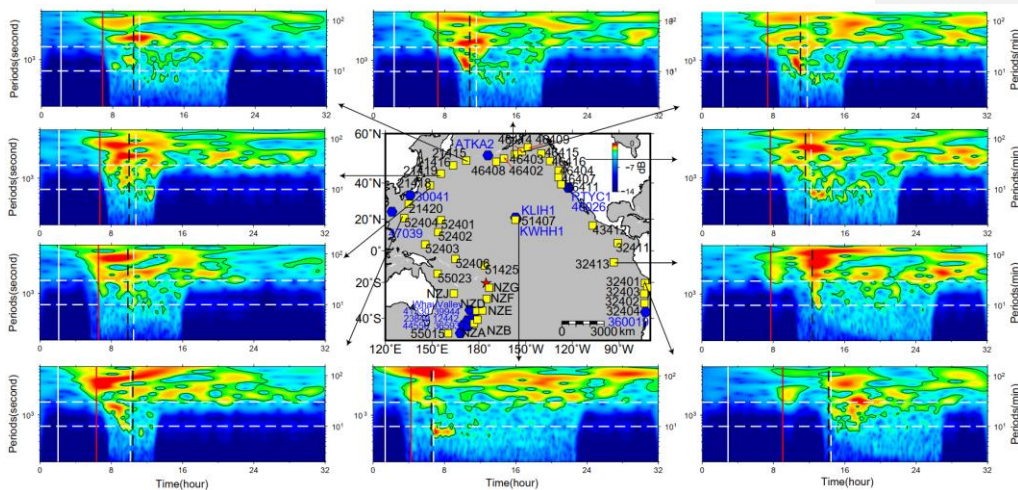
304 The tsunami components with the shortest period of ~3–5 min (stations NZE, NZF, NZG and NZJ;

305 marked with black dashed squares in Figure 5) are only observed at DART records near the eruption

14

location. Meanwhile, the arrival times of these components agree well with the modelled arrivals of conventional tsunami. Thus, we believe the observed shortest period band should originate from the seafloor crustal deformation. We further infer that this component could be generated by the partial underwater caldera collapse and/or subaerial/submarine landslide failures associated with 2022 HTHH volcanic eruption.
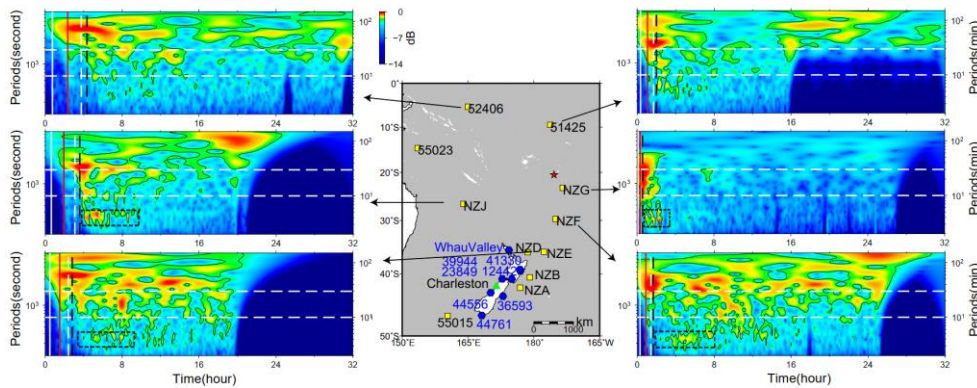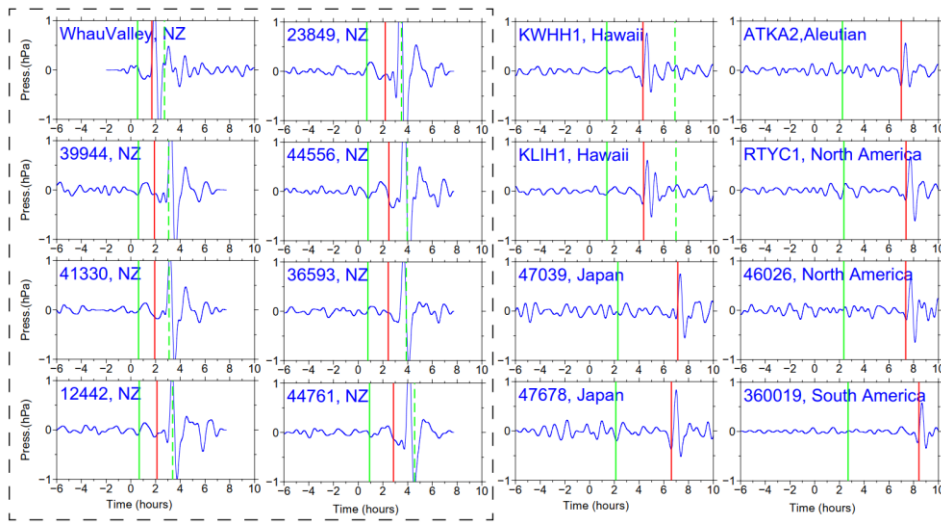

Figure 5. Wavelet analysis of representative DART buoys in the vicinity of the HTHH volcano. In each sub-plot, the solid vertical white lines mark the arrival time with travelling velocity of 1000 m/s. The solid vertical red lines mark the arrivals of Lamb waves. The dashed vertical white lines mark lower limit of AGWs' velocity of 200 m/s (Kubota et al., 2022). The dashed vertical black lines represent the theoretical tsunami arrivals. The dashed horizontal white lines mark two reference wave periods of 10 min and 30 min. The blue hexagons represent the locations of barometers. Green triangle makes the location of the tide gauges at Charleston.

15

326

327   **Figure 7. Shockwave-related atmospheric pressure waveforms of selected barometers in the Pacific**
328   **Ocean. All traces have been filtered between 30 min and 150 min. In each sub-plot, the solid vertical**
329   **green lines mark the arrival time with travelling velocity of 1000 m/s. The solid vertical red lines**
330   **mark the arrivals of Lamb waves. The dashed vertical green lines mark lower limit of AGWs'**
331   **velocity of 200 m/s.**
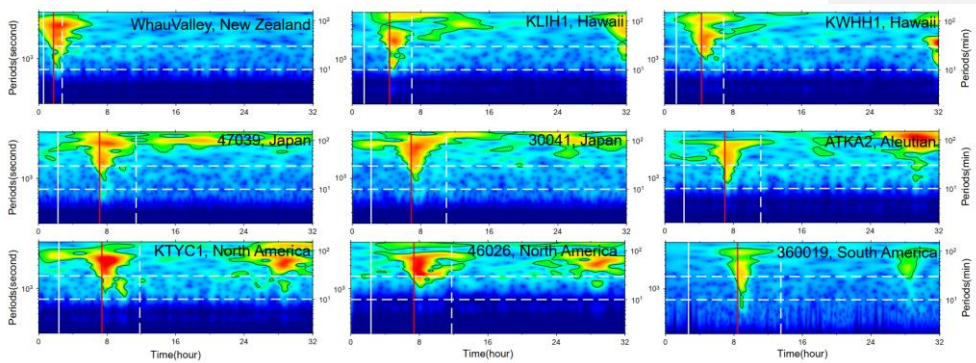
332

333   **Figure 8. Wavelet analysis of some representative barometers. In each sub-plot, the solid vertical**
334   **white lines mark the arrival time with travelling velocity of 1000 m/s. The solid vertical red lines**
335   **mark the arrivals of Lamb waves. The dashed vertical white lines mark lower limit of AGWs'**

16

velocity 200 m/s. The dashed horizontal white lines mark three reference periods of 10 min and 30 min.

4. Discussion

4.1 Tsunami from Caldera Collapse and Its Long-distance Traveling Capability

The tsunami wave energy distributed in different period bands is identified with reference arrival times. The tsunami component with 3–5 min period is most likely generated by seafloor crustal deformation in the volcanic site, but specific mechanism is not determined. A variety of possible scenarios associated with the eruption could be responsible for the near-field tsunami waves, such as volcanic earthquakes, pyroclastic flows entering the sea, underwater caldera flank collapse, and subaerial/submarine failures (Self and Rampino, 1981; Pelinovsky et al., 2005). To further investigate the source mechanism, we apply a simplified model (Rabinovich, 1997) to estimate the probable dimension of tsunami source:

$$L = \frac{T\sqrt{gH}}{2} \tag{4}$$

Where L is the typical dimension (length or width) of the tsunami source, H is average water depth in the source area, g is the gravity acceleration, and T is primary tsunami period. By comparing with the post-2015 morphology of the HTHH caldera which was obtained through drone photogrammetry and multibeam sounder surveys, Stern et al. (2022) estimate that much of the newly-formed Hunga Tonga Island and the 2014/2015 cone were destroyed by the 2022 eruption, and the vertical deformation of Hunga Ha'apai Island is ~10–15 m (Stern et al., 2022). With no more quantitative constraint of the seafloor deformation, we tentatively assume H as 10–15 m, then the possible dimension of seafloor crustal deformation responsible for the small-scale tsunami could be in the scale of 0.8–1.8 km (Figure 9a). The estimated size is very likely from partial caldera collapse that usually has limited scale in volcanic site (Ramalho et al., 2015; Omira et al., 2022). If it is the case, the partial flank collapse could be located between Hunga Tonga and Hunga Ha'apai Islands.
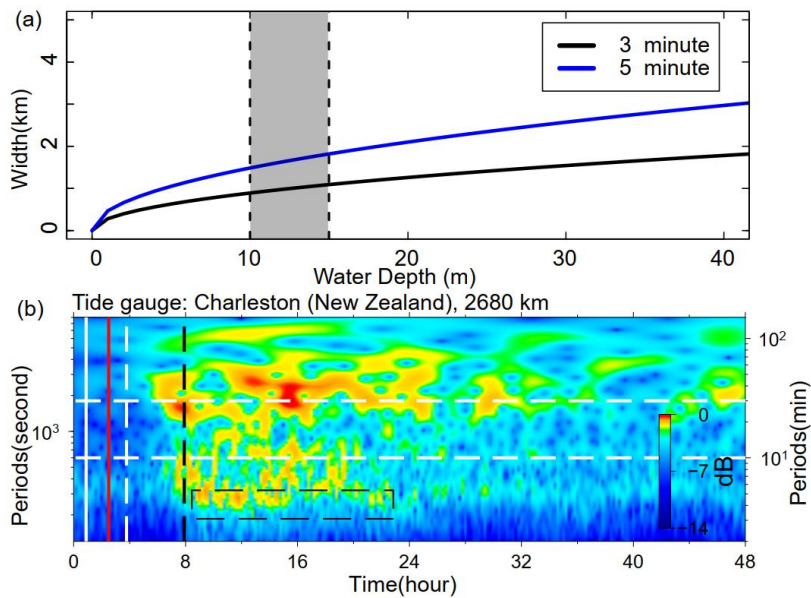
Figure 9. Mechanism of tsunami component with 3–5min period. (a) The source dimension estimated by equation 4. (b) Wavelet analysis of tide gauge at Charleston, New Zealand, 2680 km away from the eruption site. The solid vertical white line marks the arrival time with travelling velocity of 1000 m/s. The solid vertical red line marks the arrival of Lamb wave. The dashed vertical white line marks lower limit of AGWs' velocity 200 m/s. The dashed vertical black line marks the theoretical tsunami arrivals.

An interesting phenomenon is that the tsunami component with 3–5 min period can still be observed in a bay-shaped coastal area at Charleston in New Zealand (see the location in Figure 5) which is 2680 km away from the eruption site and maintains a high energy level lasting up to 14 h (Figure 9b). The long-traveling capability could be associated with the ~ 10000 m deep water depth of the Tonga Trench that keeps the source signals from substantial attenuation. In deep open ocean, the wavelength of a tsunami can reach two hundred kilometers, but the height of the tsunami may be only a few centimeters. Tsunami waves in the deep ocean can travel thousands of kilometers at high speeds, meanwhile losing very little energy in the process. The long oscillation can be attributed to the multiple reflections of the incoming waves trapped in the shallow-water bay at Charleston.

  Generally, devasting tsunamis with long-distance travelling capability are mostly generated by megathrust earthquakes (Titov et al., 2005). Caldera collapses or submarine landslides with limited scale normally only generate local tsunamis, e.g., the 1998 PNG (Papua New Guinea) tsunami event (Kawata

18

378 et al., 1999) and the 1930 Cabo Girão tsunami event (Ramalho et al., 2015). Therefore, it's exceptional

379 that the tsunami component from scale-limited failure could travel at-least 2680 km away from the

380 eruption site. It demonstrates that tsunamis from small-scale tsunamigenic source have the capability to

381 travel long distance and cause long oscillation at favored condition, e.g., deep trench, ocean ridge and

382 bay-shaped coasts.

383 **4.2 The Possible Mechanisms of Long Tsunami Oscillation**

384 An important tsunami behavior of the 2022 HTHH tsunami is the long-lasting oscillation ~ 3 days in the

385 Pacific Ocean (Figure 10a), which is comparable to that of the 2011 Tohoku tsunami, ~4 days

386 (Heidarzadeh and Satake, 2013). We demonstrate the duration time of the tsunami oscillation through

387 ARMS (Averaged-Root-Mean-Square) approach that is a measure of absolute average tsunami amplitude

388 in a time period. The long-lasting tsunami energy can be observed at many regions, such as the coasts of

389 New Zealand, Japan, Aleutian, Chile, Hawaii, and west coasts of America. Several mechanisms could

390 account for the long-lasting tsunami, including (1) Lamb waves circling the Earth multiple times

391 (Amores et al., 2022; Matoza et al., 2022), (2) resonance effect between ocean waves and atmospheric

392 waves (Kubota et al., 2022), and (3) bathymetric effect. We discuss the contribution of each mechanism

393 in the following section.

394 To investigate the contribution of Lamb wave to the long-lasting tsunami, we compare the air pressure

395 disturbances recorded by selected barometers together with the tsunami waveforms of nearby tide gauges

396 (Figure 10b). While the barometers present discernible wave pulses at each Lamb wave's arrival, only

397 the first Lamb wave triggered clear tsunami signal and no detectable tsunami signatures correspond to

398 the following passage, suggesting the Lamb waves do not directly contribute to the long oscillation.

399 Theoretically, the resonance effects between ocean waves and atmospheric waves could contribute to the

400 long oscillation on coastlines based on the following reasons. First, part of the atmospheric gravity waves

401 propagated at velocities close to averaged velocities of conventional tsunami in the Pacific Ocean (198–

402 221 m/s) which resulted in the resonance with ocean waves (Kubota et al., 2022). Second, when Lamb

403 wave speed approaches the tsunami speed, Proudman resonance gradually increase tsunami heights,

404 wherein Proudman resonance optimally maximizes tsunami heights when they match well. In deep

405 oceanic trenches, such as Mariana and Tonga-Kermadec trench (10000–11000 m), tsunami velocities

406 range between ~314–330m/s which are comparable with those of the observed Lamb waves 315–340

带格式的: 字体: 10 磅, 字体颜色: 文字 1

m/s. ~~Second, in deep oceanic trenches, such as Mariana and Tonga-Kermadec trench (10000–11000 m), tsunami velocities range between ~314–330m/s which are comparable with those of the observed Lamb waves 315–340 m/s. When Lamb wave speed approaches the tsunami speed, Proudman resonance gradually increase tsunami heights, wherein Proudman resonance optimally maximizes tsunami heights when they match well (Tanioka et al., 2022; Lynett et al., 2022).~~ Therefore, the resonance effect, could be a possible source of increased wave energy ~~continuously supplied wave energy to the ocean~~, especially in the deep trenches (Lynett et al., 2022; Tanioka et al., 2022).~~—~~

To examine the role of local bathymetry in the long-lasting tsunami, we choose a well-studied and well-recorded event: the 2011 Mw 9.0 Tohoku tsunami as a reference event and compare the tsunami records of these two events at the same coastal stations. Although the two tsunami events were generated by completely different mechanisms, i.e., large-scale seafloor deformation for the Mw 9.0 megathrust earthquake (Mori et al., 2011) and fast-moving atmospheric waves for the Mw 5.8 volcanic eruption (Matoza et al., 2022) ~~(Titov et al., 2005)~~, they both produced widespread transoceanic tsunamis which were well recorded in the Pacific DART buoys and tide gauges. In the near-field, the 2011 Tohoku earthquake produced runup up to 40 m at Miyako in the Iwate Prefecture, ~70 km from the source (Mori et al., 2011) ~~(Tanioka et al., 2022)~~, while the 2022 HTHH tsunami produced only ~13 m runup in the near field from eyewitness accounts in Kanokupolu, 60 km from the volcano (Lynett et al., 2022). However, in the far-field (>1000 km), we observe comparable tsunami wave heights in certain coastal regions. Based on the tsunami records at 21 tide gauges surrounding the Pacific Ocean, Heidarzadeh & Satake (2013) calculated the average value of the maximum tsunami heights (trough-to-crest) of the 2011 Tohoku tsunami is 1.6 m with the largest height of 3.9 m at the Coquimbo Bay in Chile (Heidarzadeh and Satake, 2013). Coincidently, the statistics of 116 tide gauges in this study also suggest the average tsunami heights of the 2022 HTHH tsunami is around the same order, ~1.2 m, among which, the largest height is 3.6 m at Chañaral Bay in Chile. Interestingly, in the coastal region of South America, the locations of the largest tsunami heights of both events are adjacent (Figure 4a), i.e., Coquimbo (the 2011 Tohoku) and Chañaral (The 2022 HTHH).

To further compare the far-field hydrodynamic processes between these two events quantitatively, we conduct wavelet analysis for four representative tide gauges distributed across the Pacific Ocean, i.e. coastal gauges at East Cape in New Zealand, Kwajalein Island, Wake Island, and Talcahuaho in Chile

436   (see their locations in Figures 10b). The temporal changes of tsunami energy of both events can be seen

437   in Figure 11. At each tide gauge, the tsunami energy of the 2011 HTHH (Figure 11a) and the 2022 Tohoku

438   tsunamis (Figure 11b) for the first few hours after the arrivals is nonuniform with different significant

439   peaks distributed within a wide period band of ~3–100 min. Then, the following long-lasting energy of

440   the both at each station presents similar pattern and is concentrated at identical and fairly narrower period

441   channel, i.e., ~20–30 min at East Cape in New Zealand, ~40–60 min at Kwajalein Island, ~10 min at

442   Wake Island, and ~100 min at Talcahuaho in Chile, which reflects the local bathymetric effects of natural

443   permanent oscillations (Hu et al., 2022; Satake et al., 2020). Specifically, many bathymetric effects can

444   contribute to the long-lasting tsunami, such as multiple reflections across the basins, or the continental

445   shelves, and the excited tsunami resonance in bays/harbors with variable shapes and sizes (Aranguiz et

446   al., 2019; Satake et al., 2020). For example, tide gauges around New Zealand are primarily distributed in

447   harbors/ports with major natural oscillation modes of ~20–30 min (De Lange and Healy, 1986; Lynett et

448   al., 2022). The first oscillation mode of central Chile is centered around ~100 min (Aranguiz et al., 2019).

449   Consequently, Figure 11 illustrates that the long-lasting tsunami energy of the two events is respectively

450   distributed in 20–30 min period at East Cape in New Zealand and in ~100 min period at Talcahuaho in

451   central Chile. The coupling of bathymetric oscillation mode with tsunami containing similar-period wave

452   results in the excitement of tsunami resonance, which amplifies tsunami waves and prolongs the tsunami

453   oscillation at the two stations (Heidarzadeh et al., 2019, 2021; Hu et al., 2022; Wang et al., 2022).

454   Simply put, we do not have clear evidence that atmospheric acoustic-gravity waves from the 2022 HTHH

455   eruption directly contribute to the long-lasting tsunami, but the resonance effect associated with ocean

456   waves could a possible source of increased wave energy and amplification~~atmospheric acoustic gravity~~

457   ~~waves from the 2022 HTHH eruption do not directly contribute to the long-lasting tsunami, but the~~

458   ~~resonance effect associated with ocean waves theoretically could contribute to it~~. However, the similarity

459   of far-filed hydrodynamic behaviors between the 2022 HTHH volcanic tsunami and the 2011 Tohoku

460   seismogenic tsunami well demonstrates the both went through similar hydrodynamic processes after their

461   arrivals. The consistency favors that the long-lasting tsunami of 2022 HTHH tsunami event can very

462   likely be attributed by the interplays between local bathymetry and conventional tsunami left after each

463   passage of atmospheric waves, which can well explain why the two completely distinct tsunami events

464   possess a comparable duration time.

带格式的: 字体: 10 磅

带格式的: 字体: 10 磅, 字体颜色: 文字 1

465
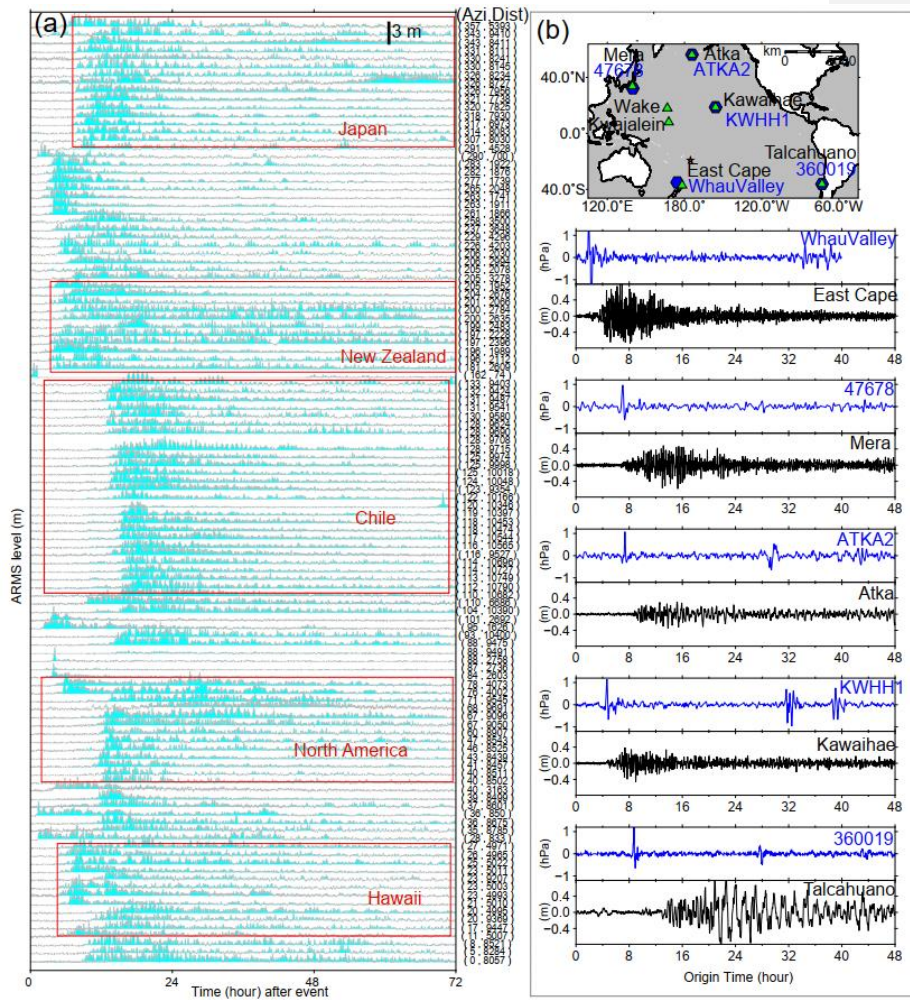
Figure 10. Tsunami duration. (a) Tsunami durations at Pacific 116 tide gauges through ARMS level
approach. (b) the location of barographs (blue curves) and nearby tide gauges (green curves), as
well as their waveforms.

469
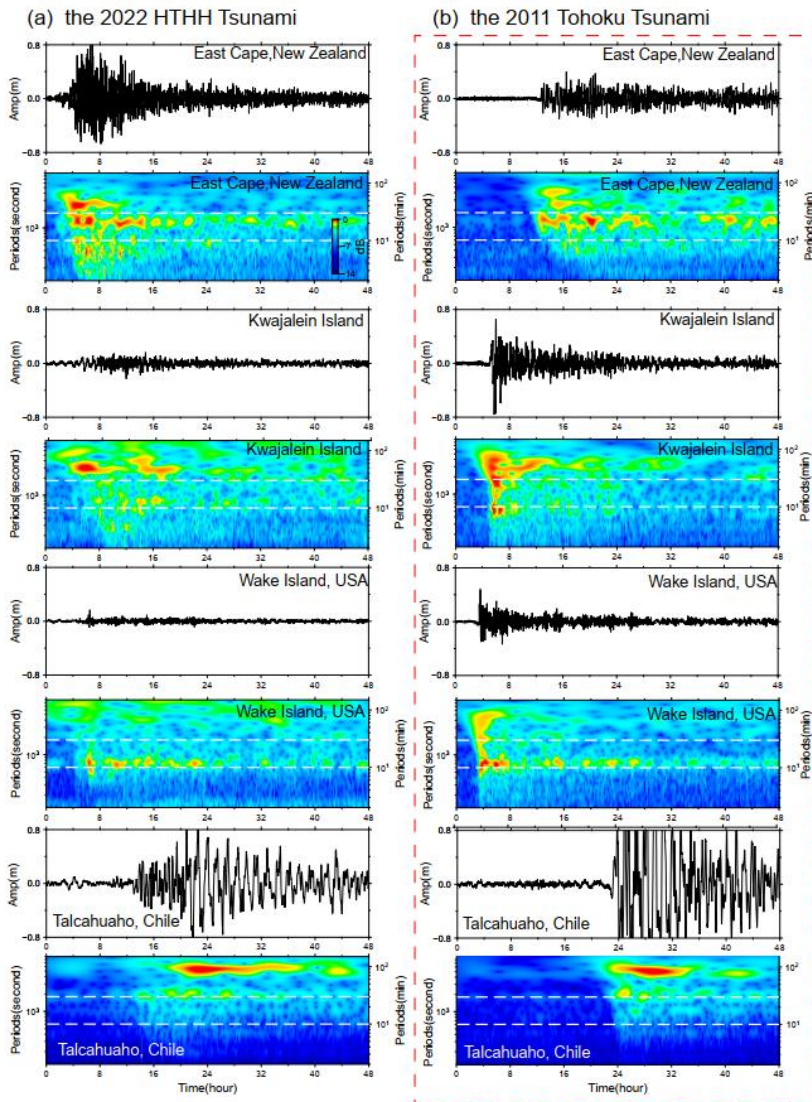
Figure 11. Wavelet analysis of tsunami waveforms recorded by 4 tide gauges during (a) the 2022 HTHH tsunami event, and (b) the 2011 Tohoku tsunami event. Horizontal white dashed lines respectively mark reference periods of 10 min and 30 min.

4.3 Challenges for Tsunami Warning

The generation mechanisms and hydrodynamic characteristics of the 2022 HTHH volcanic tsunami are more complicated than pure seismogenic tsunami, which challenge the traditional tsunami warning

23

477   approach.

478   The first challenge is posed by the tsunami components with propagating velocities faster than the

479   conventional tsunami. The Tonga volcanic tsunami event provides an excellent example which highlights

480   that the tsunamigenic mechanisms are not limited to tectonic activities related with the sudden seafloor

481   displacements, but also include a variety of atmospheric waves with distinct propagation velocities. The

482   tsunami components in 2022 HTHH event generated by the air-sea coupling possess a wide range of

483   velocities from 1000 m/s to 200 m/s. The Lamb waves recorded in both the 2022 HTHH event and the

484   1833 Krakatoa volcanic event traveled along the Earth's surface globally for several times (Carvajal et

485   al., 2022). The tsunami waves produced by Lamb waves, the wave components associated with resonance

486   of the air-sea coupling and their superimposition increase the difficulty of tsunami warning.

487   Another critical challenge is associated with the interplays between tsunami waves and local bathymetry.

488   The tsunami waves left by each passage of the atmospheric waves can interact with local bathymetry at

489   coastlines, such as continental shelves with different slopes, and harbor/bay with different shapes and

490   sizes. The interaction can intensify the tsunami impact and excite a variety of natural oscillation periods.

491   The 2022 HTHH tsunami with an extremely wide period range of ~2–100 min have a great potential to

492   couple with the excited natural oscillations and form extensive tsunami resonance phenomena. The

493   resonance effects result in long-lasting oscillation and delayed tsunami wave peaks. The uncertain

494   arrivals of the maximum tsunami waves pose an extra challenge to tsunami warning.

495 **5. Conclusion**

496   In the study, we explore the tsunamigenic mechanisms and the hydrodynamic characteristics of the 2022

497   HTHH volcanic tsunami event. Through extensive analysis of waveforms recorded by the DART buoys,

498   tide gauges and barometers in the Pacific Ocean, we reach the main findings as follows:

499   (1) We identify four distinct tsunami wave components based on their distinct propagation velocities or

500   period bands (~80–100 min, 10–30 min, 30–40 min, and 3–5 min). The generation mechanisms of these

501   tsunami components range from air-sea coupling to seafloor crustal deformation during the volcanic

502   eruption.

503   (2) The first-arriving tsunami component with 80–100 min period was most likely from shock wave

504   spreading at a velocity of ~1000 m/s in the vicinity of the eruption. This tsunami component was not

505 clearly identified by currently available publication and it's not easy to be visually observed through time

506 series of the waveforms. The physical mechanism is yet to be understood. The second tsunami component

507 with 30–40 min period was from Lamb waves, and was the most discussed tsunami source of this event

508 so far. A thorough analysis of DART measurements indicates that the Lamb waves traveled at the speed

509 of ~340 m/s in the vicinity of the eruption and decreased to ~315 m/s when traveling away due to cooling

510 of the air temperature. The third tsunami component was from some atmospheric gravity wave modes

511 with propagation velocity faster than 200 m/s but slower than Lamb waves. The last tsunami component

512 with the shortest periods 3-5 min was probably produced by partial caldera collapse with estimated

513 dimension of ~0.8–1.8 km.

514 (3) Although the resonance effect with the atmospheric acoustic-gravity waves theoretically could be a

515 source of increased wave energy, its direct contribution to the long-lasting oscillation is not demonstrated

516 yet. However, the comparison of hydrodynamical characteristics between the 2022 HTHH tsunami event

517 and the 2011 Tohoku tsunami event well demonstrated that the interactions between the ocean waves left

518 by atmospheric waves and local bathymetry contribute to the long-lasting Pacific oscillation of the 2022

519 tsunami event. The long-lasting Pacific oscillation of this tsunami event was not only associated with the

520 resonance effect with the atmospheric acoustic-gravity waves, but more importantly the interactions with

521 local bathymetry. The velocities of tsunami waves in deep ocean (especially at Mariana and Tonga-

522 Kermadec trenches) close to those of acoustic Lamb waves and some gravity wave modes produced

523 resonance effects, which supplied energy to the ocean. The comparison of hydrodynamical characteristics

524 between the 2022 HTHH tsunami event and the 2011 Tohoku tsunami event suggests the volcanic

525 tsunami oscillation was prolonged by their interplays with local bathymetry.

526 (4) The extraordinary features of this rare volcanic tsunami event challenge the current tsunami warning

527 system which is mainly designed for seismogenic tsunamis. It is necessary to improve the awareness of

528 people at risks about the potential tsunami hazards associated with volcanic eruptions. New approaches

529 are expected to be developed for tsunami hazard assessments with these unusual sources: various

530 atmospheric waves radiated by volcanic eruptions besides those traditionally recognized, e.g.

531 earthquakes, landslides, caldera collapses and pyroclastic flows etc.

带格式的: 字体: 10 磅, 字体颜色: 文字 1

带格式的: 字体: 10 磅, 字体颜色: 文字 1

Reference

Adam, D.: Tonga volcano created puzzling atmospheric ripples, Nature, https://doi.org/10.1038/d41586-022-00127-1, 2022.

Amores, A., Monserrat, S., Marcos, M., Argüeso, D., Villalonga, J., Jordà, G., and Gomis, D.: Numerical simulation of atmospheric Lamb waves generated by the 2022 Hunga-Tonga volcanic eruption, Geophys. Res. Lett., 49, e2022GL098240, https://doi.org/10.1029/2022GL098240, 2022.

Aranguiz, R., Catalán, P. A., Cecioni, C., Bellotti, G., Henriquez, P., and González, J.: Tsunami Resonance and Spatial Pattern of Natural Oscillation Modes With Multiple Resonators, J. Geophys. Res. Ocean., 124, 7797–7816, https://doi.org/10.1029/2019JC015206, 2019.

Baba, T., Takahashi, N., Kaneda, Y., Ando, K., Matsuoka, D., and Kato, T.: Parallel Implementation of Dispersive Tsunami Wave Modeling with a Nesting Algorithm for the 2011 Tohoku Tsunami, Pure

560   Appl. Geophys., 172, 3455–3472, https://doi.org/10.1007/s00024-015-1049-2, 2015.

561   Bevis, M., Taylor, F. W., Schutz, B. E., Recy, J., Isacks, B. L., Helu, S., Singh, R., Kendrick, E.,

562   Stowell, J., Taylor, B., and Calmantli, S.: Geodetic observations of very rapid convergence and back-

563   arc extension at the tonga arc, Nature, 374, 249–251, https://doi.org/10.1038/374249a0, 1995.

564   Billen, M. I., Gurnis, M., and Simons, M.: Multiscale dynamics of the Tonga–Kermadec subduction

565   zone, Geophys. J. Int., 153, 359–388, https://doi.org/10.1046/j.1365-246X.2003.01915.x, 2003, 2003.

566   Carvajal, M., Sepúlveda, I., Gubler, A., and Garreaud, R.: Worldwide Signature of the 2022 Tonga

567   Volcanic Tsunami, Geophys. Res. Lett., 49, e2022GL098153, https://doi.org/10.1029/2022GL098153,

568   2022.

569   Duncombe, J.: The Surprising Reach of Tonga's Giant Atmospheric Waves.pdf, Eos (Washington.

570   DC)., 103, https://doi.org/10.1029/2022EO220050, 2022.

571   E. E. Gossard and W. H. Hooke: Waves in the Atmosphere: Atmospheric Infrasound and Gravity

572   Waves—Their Generation and Propagation, Elsevier, 1975.

573   Edmonds, M.: Hunga-Tonga-Hunga-Ha'apai in the south Pacific erupts violently, Temblor,

574   https://doi.org/10.32858/temblor.231, 2022.

575   Garvin, J. B., Slayback, D. A., Ferrini, V., Frawley, J., Giguere, C., Asrar, G. R., and Andersen, K.:

576   Monitoring and Modeling the Rapid Evolution of Earth's Newest Volcanic Island: Hunga Tonga

577   Hunga Ha'apai (Tonga) Using High Spatial Resolution Satellite Observations, Geophys. Res. Lett., 45,

578   3445–3452, https://doi.org/10.1002/2017GL076621, 2018.

579   Gossard, E. E. and Hooke, W. H.: Waves in the Atmosphere, Amsterdam: Elsevier, 1975.

580   Heidarzadeh, M. and Satake, K.: Waveform and Spectral Analyses of the 2011 Japan Tsunami Records

581   on Tide Gauge and DART Stations Across the Pacific Ocean, Pure Appl. Geophys., 170, 1275–1293,

582   https://doi.org/10.1007/s00024-012-0558-5, 2013.

583   Heidarzadeh, M. and Satake, K.: Excitation of Basin-Wide Modes of the Pacific Ocean Following the

584   March 2011 Tohoku Tsunami, Pure Appl. Geophys., 171, 3405–3419, https://doi.org/10.1007/s00024-

585   013-0731-5, 2014.

586   Hu, G., Feng, W., Wang, Y., Li, L., He, X., Karakaş, Ç., and Tian, Y.: Source characteristics and

587   exacerbated tsunami hazard of the 2020 Mw 6.9 Samos earthquake in eastern Aegean Sea, J. Geophys.

588   Res.   Solid Earth, 127, e2022JB023961, https://doi.org/10.1029/2022JB023961, 2022.

Kawata, Y., Benson, B. C., Borrero, J. C., Borrero, J. L., Davies, H. L., Lange, W. P. de, Imamura, F., Letz, H., Nott, J., and Synolakis, C. E.: Tsunami in Papua New Guinea Was as Intense as First Thought, Eos, Trans. Am. Geophys. Union, 80, 9, https://doi.org/10.1029/99EO00065, 1999.

Kristeková, M., Kristek, J., Moczo, P., and Day, S. M.: Misfit Criteria for Quantitative Comparison of Seismograms, Bull. Seismol. Soc. Am., 96, 1836–1850, https://doi.org/10.1785/0120060012, 2006.

Kubota, T., Saito, T., and Nishida, K.: Global fast-traveling tsunamis by atmospheric pressure waves on the 2022 Tonga eruption, Science (80-.)., https://doi.org/10.1126/science.abo4364, 2022.

Kulichkov, S. N., Chunchuzov, I. P., Popov, O. E., Gorchakov, G. I., Mishenin, A. A., Perepelkin, V. G., Bush, G. A., Skorokhod, A. I., Yu. A. Vinogradov, Semutnikova, E. G., Šepic, J., Medvedev, I. P., Gushchin, R. A., Kopeikin, V. M., Belikov, I. B., Gubanova, D. P., and A. V. Karpov & A. V. Tikhonov: Acoustic-Gravity Lamb Waves from the Eruption of the Hunga-Tonga-Hunga-Hapai Volcano, Its Energy Release and Impact on Aerosol Concentrations and Tsunami, Pure Appl. Geophys., https://doi.org/10.1007/s00024-022-03046-4, 2022.

De Lange, W. P. and Healy, T. R.: New Zealand tsunamis 1840–1982, New Zeal. J. Geol. Geophys., 29, 115–134, https://doi.org/10.1080/00288306.1986.10427527, 1986.

Lin, J., Rajesh, P. K., Lin, C. C. H., Chou, M., Liu, J.-Y., Yue, J., Hsiao, T.-Y., Tsai, H.-F., Chao, H.-M., and Kung, M.-M.: Rapid Conjugate Appearance of the Giant Ionospheric Lamb Wave Signatures in the Northern Hemisphere After Hunga- Tonga Volcano Eruptions, Geophys. Res. Lett., 49, e2022GL098222, https://doi.org/10.1029/2022GL098222, 2022.

Liu, P. L.-F. and Higuera, P.: Water waves generated by moving atmospheric pressure : Theoretical analyses with applications to the 2022 Tonga event, arXiv Prepr., https://doi.org/10.48550/arXiv.2205.05856, 2022.

Liu, X., Xu, J., Yue, J., and Kogure, M.: Strong Gravity Waves Associated With Tonga Volcano Eruption Revealed by SABER Observations, Geophys. Res. Lett., 49, e2022GL098339, https://doi.org/10.1029/2022GL098339, 2022.

Lynett, P., McCann, M., Zhou, Z., Renteria, W., Borrero, J., Greer, D., Fa'anunu, 'Ofa, Bosserelle, C., Jaffe, B., Selle, S. La, Ritchie, A., Snyder, A., Nasr, B., Bott, J., Graehl, N., Synolakis, C., Ebrahimi, B., and Cinar, E.: The Tsunamis Generated by the Hunga Tonga- Hunga Ha ' apai Volcano on January 15 , 2022, ResearchSquare, https://doi.org/10.21203/rs.3.rs-1377508/v1, 2022.

618 Matoza, R. S., Matoza, R. S., Fee, D., Assink, J. D., Iezzi, A. M., Green, D. N., Kim, K., Lecocq, T.,

619 Krishnamoorthy, S., Lalande, J., Nishida, K., and Gee, K. L.: Atmospheric waves and global

620 seismoacoustic observations of the January 2022 Hunga eruption ,Tonga, Science (80-.).,

621 https://doi.org/10.1126/science.abo7063, 2022.

622 Mori, N., Takahashi, T., Yasuda, T., and Yanagisawa, H.: Survey of 2011 Tohoku earthquake tsunami

623 inundation and run-up, Geophys. Res. Lett., 38, L00G14, https://doi.org/10.1029/2011GL049210,

624 2011.

625 NASA: National Aeronautics and Space Administration,"Dramatic changes at Hunga Tonga-Hunga

626 Ha'apai," 2022.

627 Nomanbhoy, N. and Satake, K.: Generation mechanism of tsunamis from the 1883 Krakatau Eruption,

628 Geophys. Res. Lett., 22, 509–512, https://doi.org/10.1029/94GL03219, 1995.

629 Omira, R., Baptista, M. A., Quartau, R., Ramalho, R. S., Kim, J., Ramalho, I., and Rodrigues, A.: How

630 hazardous are tsunamis triggered by small-scale mass-wasting events on volcanic islands ? New

631 insights from Madeira–NE Atlantic, Earth Planet. Sci. Lett., 578, 117333,

632 https://doi.org/10.1016/j.epsl.2021.117333, 2022.

633 Otsuka, S.: Visualizing Lamb Waves From a Volcanic Eruption Using Meteorological Satellite

634 Himawari-8, Geophys. Res. Lett., 49, e2022GL098324, https://doi.org/10.1029/2022GL098324, 2022.

635 Pelinovsky, E., Choi, B. H., Stromkov, A., Didenkulova, I., and Kim, H.: Analysis of Tide-Gauge

636 Records of the 1883 Krakatau Tsunami. In: Satake, K. (eds) Tsunamis, Adv. Nat. Technol. Hazards

637 Res., 23, Springer, Dordrech, https://doi.org/10.1007/1-4020-3331-1_4, 2005.

638 Plank, S., Marchese, F., Genzano, N., Nolde, M., and Martinis, S.: The short life of the volcanic island

639 New Late'iki (Tonga) analyzed by multi-sensor remote sensing data, Sci. Rep., 10, 22293,

640 https://doi.org/10.1038/s41598-020-79261-7, 2020.

641 Rabinovich, A. B.: Spectral analysis of tsunami waves: Separation of source and topography effects, J.

642 Geophys. Res. Ocean., 102, 12663–12676, https://doi.org/10.1029/97JC00479, 1997.

643 Rabinovich, A. B.: Seiches and harbor oscillations. in: Handbook of coastal and ocean engineering, pp,

644 193–236, 2009.

645 Rabinovich, A. B., Thomson, Æ. R. E., and Stephenson, F. E.: The Sumatra tsunami of 26 December

646 2004 as observed in the North Pacific and North Atlantic oceans, Surv. Geophys., 27, 647–677,

647   https://doi.org/10.1007/s10712-006-9000-9, 2006.

648   Rabinovich, A. B., Titov, V. V., Moore, C. W., and Eble, M. C.: The 2004 Sumatra Tsunami in the

649   Southeastern Pacific Ocean: New Global Insight From Observations and Modeling, J. Geophys. Res.

650   Ocean., 122, 7992–8019, https://doi.org/https://doi.org/10.1002/2017JC013078, 2017.

651   Ramalho, R. S., Winckler, G., Madeira, J., Helffrich, G. R., Hipólito, A., Quartau, R., Adena, K., and

652   Schaefer, J. M.: Hazard potential of volcanic flank collapses raised by new megatsunami evidence, Sci.

653   Adv., 1, e1500456, https://doi.org/10.1126/sciadv.1500456, 2015.

654   Ramírez-Herrera, M. T., Coca, O., and Vargas-Espinosa, V.: Tsunami Effects on the Coast of Mexico

655   by the Hunga Tonga-Hunga Ha'apai Volcano, Pure Appl. Geophys., https://doi.org/10.1007/s00024-

656   022-03017-9, 2022.

657   Satake, K.: Earthquakes: Double trouble at Tonga, Nature, 466, 931–932,

658   https://doi.org/10.1038/466931a, 2010.

659   Satake, K., Heidarzadeh, M., Quiroz, M., and Cienfuegos, R.: History and features of trans-oceanic

660   tsunamis and implications for paleo-tsunami studies, Earth-Science Rev., 202, 103112,

661   https://doi.org/10.1016/j.earscirev.2020.103112, 2020.

662   Self, S. and Rampino, M. R.: K-1981Self_Nature_The 1883 eruption of Krakatau, Nature, 294, 699–

663   704, https://doi.org/10.1038/294699a0, 1981.

664   Stern, S., Cronin, S., Ribo, M., Barker, S., Brenna, M., Smith, I. E. M., Ford, M., Kula, T., and

665   Vaiomounga, R.: Post-2015 caldera morphology of the Hunga Tonga-Hunga Ha ' apai caldera ,

666   Tonga , through drone photogrammetry and summit area bathymetry, EGU Gen. Assem. 2022,

667   https://doi.org/10.5194/egusphere-egu22-13586, 2022.

668   Tanioka, Y., Yamanaka, Y., and Nakagaki, T.: Characteristics of the deep sea tsunami excited offshore

669   Japan due to the air wave from the 2022 Tonga eruption, Earth, Planets Sp., 74, 61,

670   https://doi.org/10.1186/s40623-022-01614-5, 2022.

671   Themens, D. R., Watson, C., Žagar, N., Vasylkevych, S., Elvidge, S., McCaffrey, A., Prikryl, P., Reid,

672   B., Wood, A., and Jayachandran, P. T.: Global Propagation of Ionospheric Disturbances Associated

673   With the 2022 Tonga Volcanic Eruption, Geophys. Res. Lett., 49, e2022GL098158,

674   https://doi.org/10.1029/2022GL098158, 2022.

675   Titov, V., Rabinovich, A. B., Mofjeld, H. O., Thomson, R. E., and Gonza, F. I.: The Global Reach of

676   the 26 December 2004 Sumatra Tsunami, Science (80-.)., 309, 2045–2049,

677   https://doi.org/10.1126/science.1114576, 2005.

678   USGS: M 5.8 Volcanic Eruption - 68 km NNW of Nukuʻalofa, Tonga, U.S. Geol. Surv., 2022.

679   Wang, Y., Heidarzadeh, M., Satake, K., Mulia, I. E., and Yamada, M.: A Tsunami Warning System

680   Based on Offshore Bottom Pressure Gauges and Data Assimilation for Crete Island in the Eastern

681   Mediterranean Basin, J. Geophys. Res. Solid Earth, 125, e2020JB020293,

682   https://doi.org/10.1029/2020JB020293, 2020.

683   Wang, Y., Zamora, N., Quiroz, M., Satake, K., and Cienfuegos, R.: Tsunami Resonance

684   Characterization in Japan Due to Trans-Pacific Sources: Response on the Bay and Continental Shelf, J.

685   Geophys. Res. Ocean., 126, 1–16, https://doi.org/10.1029/2020JC017037, 2021.

686   Wang, Y., Heidarzadeh, M., Satake, K., and Hu, G.: Characteristics of two tsunamis generated by

687   successive Mw 7.4 and Mw 8.1 earthquakes in Kermadec Islands on March 4,2021, Nat. Hazards Earth

688   Syst. Sci., 22, 1–10, https://doi.org/10.5194/nhess-2021-369, 2022.

689   Yuen, D. A., Scruggs, M. A., Spera, F. J., Yingcai Zheng, Hao Hu, McNutt, S. R., Glenn Thompson,

690   Mandli, K., Keller, B. R., Wei, S. S., Peng, Z., Zhou, Z., Mulargia, F., and Tanioka1, Y.: Under the

691   Surface: Pressure-Induced Planetary-Scale Waves, Volcanic Lightning, and Gaseous Clouds Caused by

692   the Submarine Eruption of Hunga Tonga-Hunga Ha'apai Volcano Provide an Excellent Research

693   Opportunity, Earthq. Res. Adv., https://doi.org/10.1016/j.eqrea.2022.100134, 2022.

694   Zhang, S., Vierinen, J., Aa, E., Goncharenko, L. P., Erickson, P. J., Rideout, W., Coster, A. J., and

695   Spicher, A.: 2022 Tonga Volcanic Eruption Induced Global Propagation of Ionospheric Disturbances

696   via Lamb Waves, Front. Astron. Sp. Sci., 9, 1–10, https://doi.org/10.3389/fspas.2022.871275, 2022.

697